The vanadium isotopic composition of lunar basalts

S.S. Hopkins [a,*], J. Prytulak [b,c], J. Barling [a], S.S. Russell [d], B.J. Coles [b], A.N. Halliday [a,e]

[a] *Department of Earth Sciences, University of Oxford, OX1 3AN, United Kingdom*
[b] *Department of Earth Sciences and Engineering, Imperial College, London, SW7 2AZ, United Kingdom*
[c] *Department of Earth Sciences, Durham University, DH1 3LE, United Kingdom*
[d] *Natural History Museum, London, SW7 5BD, United Kingdom*
[e] *The Earth Institute, Columbia University, Hogan Hall, 2910 Broadway, New York, NY 10025, USA*

ABSTRACT

We present the first high-precision vanadium (V) isotope data for lunar basalts. Terrestrial magmatic rock measurements can display significant V isotopic fractionation (particularly during (Fe, Ti)oxide crystallisation), but the Earth displays heavy V (i.e. higher $^{51}V/^{50}V$) isotopic compositions compared to meteorites. This has been attributed to early irradiation of meteorite components or nucleosynthetic heterogeneity. The Moon is isotopically-indistinguishable from the silicate Earth for many refractory elements and is expected to be similar in its V isotopic composition.

Vanadium isotope ratios and trace element concentrations were measured for 19 lunar basalt samples. Isotopic compositions are more variable ($\sim$2.5‰) than has been found thus far for terrestrial igneous rocks and extend to lighter values. Magmatic processes do not appear to control the V isotopic composition, despite the large range in oxide proportions in the suite. Instead, the V isotopic compositions of the lunar samples are lighter with increasing exposure age (t_e). Modelling nuclear cross-sections for V production and burnout demonstrates that cosmogenic production may affect V isotope ratios via a number of channels but strong correlations between V isotope ratios and t_e* [Fe]/[V] implicate Fe as the primary target element of importance. Similar correlations are found in the latest data for chondrites, providing evidence that most V isotope variation in chondrites is due to recent cosmogenic production via Fe spallation. Contrary to previous suggestions, there is no evidence for resolvable differences between the primary V isotopic compositions of the Earth, Moon, chondrites and Mars.

© 2019 The Author(s). Published by Elsevier B.V. This is an open access article under the CC BY license (http://creativecommons.org/licenses/by/4.0/).

1. Introduction

1.1. Lunar origin

The most widely-accepted theory of lunar origin is the so-called "giant impact" model whereby a smaller planetary object struck the proto-Earth in its final stages of accretion leading to an impact-generated disk from which the Moon formed (Cameron and Ward, 1976; Hartmann and Davis, 1975). The model satisfies constraints on the geodynamical properties, planetary densities, and broad chemical features of the Earth-Moon system. In early numerical simulations of the giant impact most of the Moon-forming material derives from the impactor, with only a small contribution from Earth (e.g. Canup, 2004). Extra-terrestrial bodies typically have distinct isotopic compositions (Goderis et al.,

2016), thus it was assumed that the Moon should also be isotopically distinct. The Earth and the Moon are remarkably similar in mass-independent isotope variations such as ^{54}Cr (Lugmair and Shukolyukov, 1998; Mougel et al., 2018), ^{50}Ti (Zhang et al., 2012), ^{17}O (Young et al., 2016) and ^{96}Zr (Akram and Schonbachler, 2016), mass-dependent isotope variations of moderately refractory element such as Si (Armytage et al., 2012), Cr (Bonnand et al., 2016), Ti (Millet et al., 2016), Fe (Sossi and Moynier, 2017; Liu et al., 2010; Wiesli et al., 2003), and in radiogenic ^{182}W (Kruijer et al., 2015).

Several explanations have been advanced for the unexpected isotopic similarity between the Earth and the Moon. In the aftermath of a giant impact, a re-equilibration of isotopes between the Earth and newly-forming Moon might have taken place (Pahlevan and Stevenson, 2007). However, the timescales and temperatures of re-equilibration do not favour isotopic homogenisation of refractory elements – e.g. Cr and Ti. Predicted isotopic offsets in silicon based upon this model (Pahlevan et al., 2011) were not found (Armytage et al., 2012). Alternative impact scenarios have been proposed to reconcile the isotopic similarity of the Earth

---

* Corresponding author.
  E-mail address: sean.hopkins@stx.ox.ac.uk (S.S. Hopkins).

and the Moon. These include high-energy impacts (Canup, 2012; Cuk and Stewart, 2012), a hit-and-run model (Reufer et al., 2012), and a multiple-impact scenario (Rufu et al., 2017). Compared to the canonical model, each of these scenarios invokes restricted dynamic conditions prior, or subsequent, to impact.

Models of an impactor with Earth-like isotopic composition (Dauphas et al., 2014), and models of inner Solar System homogeneity have also been proposed (Mastrobuono-Battisti et al., 2015). These studies argue against the assumption of an isotopically-distinct impactor. However, a consensus on the best model of lunar formation has yet to be reached.

1.2. Chemical and isotopic variations in lunar basalts

Lunar basalts are primarily divided by TiO_2 contents into very-low-Ti basalts (VLT) (<1.5 wt% TiO_2), low-Ti basalts (1.5–6 wt% TiO_2) and high-Ti basalts (>6 wt% TiO_2). Chemically-distinct regions of the lunar mantle must exist to explain the compositional diversity of mare basalts (Papike et al., 1976), with high-Ti basalts requiring significant amounts of ilmenite in their sources. Lunar mantle heterogeneities arise from the differentiation of the lunar magma ocean (LMO), a global melting of the lunar mantle as a result of accretion, during which differentially-dense regions of the mantle inefficiently mixed as crystallisation proceeded (Elkins-Tanton et al., 2011). Stable isotope studies of lunar basalts have not only provided evidence of the isotopic kinship between the Moon and the Earth, but also the extent of lunar mantle heterogeneity, the provenance of lunar sample subsets and the nature of lunar differentiation processes. For example, high-Ti basalts show light Mg (Sedaghatpour et al., 2013), and heavy Fe and Ti isotope ratios (Liu et al., 2010; Sossi and Moynier, 2017; Wiesli et al., 2003). These isotopic differences are thought to relate to crystallisation of ilmenite during LMO differentiation, or partial melting during formation of high-Ti and low-Ti parental melts. In contrast, Cr isotope ratios show mass-dependent fractionations correlating with indices of magmatic differentiation, but no difference between high-Ti and low-Ti basalts (Bonnand et al., 2016). Fractionations in Cr isotopes result from crystallisation of Cr-spinel and Cr-bearing ülvospinel. Post-crystallisation processes can modify isotopic compositions further (in a mass-independent fashion), and lead to difficulty in identifying the original isotopic signatures of the samples. For example, small excesses in ^{53}Cr and ^{54}Cr (Mougel et al., 2018) and depletions in $\varepsilon^{50}Ti$ (Zhang et al., 2012) have been found in mare basalts, reflecting cosmogenic processes at the lunar surface.

1.3. Vanadium

Vanadium occurs in multiple oxidation states (V^{2+}, V^{3+}, V^{4+}, V^{5+}) and behaves as a moderately incompatible element in terrestrial igneous systems. Previous studies have taken advantage of the strongly redox-dependent behaviour of V to investigate oxidation states of mantle and melts throughout Earth's history (e.g. Canil, 1997; Lee et al., 2003; Lee et al., 2005, 2004; Mallmann and O'Neill, 2009; Wood et al., 2008). Vanadium is depleted in the Earth's mantle compared to CI chondrites (McDonough and Sun, 1995), and its abundance relative to siderophile elements has been used to argue for changes in mantle oxidation during Earth's accretion and core formation (Wood et al., 2008). The lunar and terrestrial upper mantles are estimated to have similar V contents (79 ppm and 81 ppm, respectively; Seifert and Ringwood, 1988). Vanadium is incompatible in plagioclase, and so is unaffected by anorthite crystallisation during LMO differentiation. Differing oxygen fugacity (fO_2) of planetary mantles can affect the partitioning behaviour of V. For example, at low lunar fO_2, 1 to 2 log units below the Iron–Wüstite buffer (IW-1 to IW-2) most V is present

in lunar magmas as V^{3+}. Vanadium is more compatible in lunar olivine, pyroxene, and spinel than for terrestrial analogues, where V^{4+} is the major species (Papike et al., 2005). The multiple valence states of V over a wide range of fO_2 makes it attractive as a potential tracer of planetary magmatic processes.

1.4. Vanadium isotopes

Vanadium has two stable isotopes: ^{50}V (0.25%) and ^{51}V (99.75%) and has been of cosmochemical interest for decades, due to the hypothesis that ^{50}V could be generated by cosmic ray irradiation processes (Stauffer and Honda, 1961). Advances in high precision multiple collector inductively-coupled-plasma mass spectrometry (MC-ICPMS) and the development of more effective separation procedures (e.g. Nielsen et al., 2011; Wu et al., 2016) now allow V isotope determination to precisions useful for geological applications ($\sim$0.2‰). Vanadium isotopes are reported in per mil (‰) deviation relative to an Alfa Aesar (AA) V solution standard introduced by Nielsen et al. (2011):

$$\delta^{51}V_{AA} = \left\{ \frac{(^{51}V/^{50}V)_{sample}}{(^{51}V/^{50}V)_{AA}} - 1 \right\} \times 1000$$

Terrestrial magmatic samples show a range of $\sim$2.3‰ in $\delta^{51}V$. This variability has been interpreted in terms of equilibrium fractionation (Prytulak et al., 2011; Prytulak et al., 2013; Prytulak et al., 2017; Wu et al., 2018, Fig. 1). The bulk silicate Earth (BSE) is estimated at $\delta^{51}V_{AA} = -0.7 \pm 0.2$‰ based on analyses of bulk peridotites (Prytulak et al., 2013), although more recent work suggests a lighter BSE ($\delta^{51}V = -0.91 \pm 0.05$, 2SD; Qi et al., 2018). Metal–silicate experiments suggest terrestrial core formation does not significantly fractionate V isotopes (Nielsen et al., 2014). Much of the variation in magmatic samples has been proposed to result from crystallisation of (Fe,Ti) oxides during magmatic differentiation (Prytulak et al., 2017; Sossi et al., 2018; Wu et al., 2018). The similarity in whole rock $\delta^{51}V$ variation with respect to indicators of magmatic evolution in two cogenetic lava suites with disparate redox conditions (Hekla, Iceland and Anatahan, Mariana arc) suggests crystallisation of (Fe,Ti) oxides and the coordination difference between melt and mineral are dominant in driving isotope fractionation rather than $\delta^{51}V$ variation directly reflecting changes in oxidation state (Prytulak et al., 2017). Recent experimental work directly determining V magnetite–melt isotope fractionation factors ($\Delta^{51}V_{magnetite-melt}$) at variable, controlled redox conditions yields $\Delta^{51}V_{magnetite-melt}$ consistent with those needed to explain the variation seen in $\sim$ closed system crystallisation and resulting Rayleigh isotope fractionation (Sossi et al., 2018). Interestingly, Sossi et al. (2018) also observed a strong positive relationship between the magnitude of $\Delta^{51}V_{magnetite-melt}$ and fO_2.

Initial analyses of chondrites, achondrites and martian meteorites returned a restricted range of $\delta^{51}V$ compositions ($\delta^{51}V_{AA} = -1.7 \pm 0.2$) uniformly-lighter than BSE (Nielsen et al., 2014). This was suggested to be due to incorporation of irradiated components in meteorites. However, more recent analyses of chondrites with medium-resolution mass spectrometry (M/ΔM $>$ 4000) suggests a revised isotopically-heavier composition for chondrites ($\delta^{51}V_{AA}$ between -1.35 to -1.05‰ for all chondrites except Xinglongquan, $\delta^{51}V = -1.76 \pm 0.05$‰; Xue et al., 2018; Nielsen et al., 2019) and martian meteorites ($\delta^{51}V_{AA} = -1.3$ to -0.7‰; Davis et al., 2018) (Fig. 1). Nielsen et al. (2019) suggest that incomplete resolution of mass interferences (e.g. polyatomic S interferences) during analyses of extra-terrestrial samples resulted in inaccurate and light $\delta^{51}V$ values for initial studies of meteorites, which were performed at lower-resolution (Nielsen et al., 2014; Prytulak et al., 2011). At medium-resolution (e.g. Wu et al., 2016; Nielsen et al., 2016) these
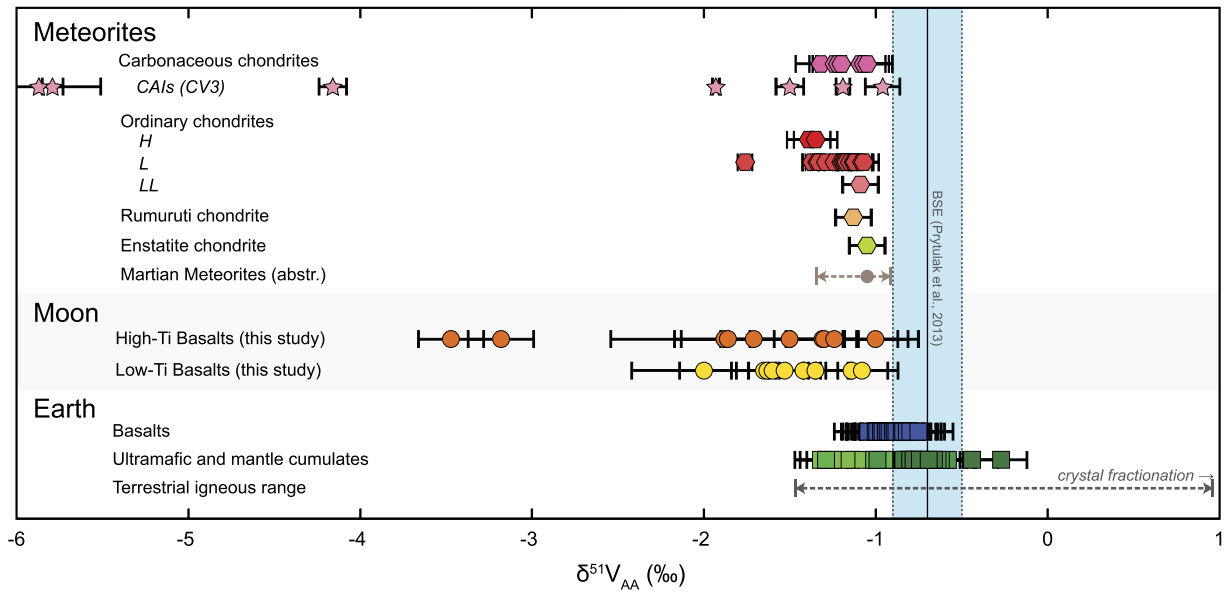
Fig. 1. Compilation of published V isotope data for Solar System materials including the lunar basalts measured in this study. Lunar basalts vary more widely in composition than all other samples, except CAIs (Sossi et al., 2017). Some CAIs show the isotopically-lightest values measured in the Solar System. Published data for chondrites is from Xue et al. (2018) and Nielsen et al. (2019) Recent data for Martian meteorites (presented only in abstract form) is included (Davis et al., 2018). The BSE estimate is indicated by the blue bar (Prytulak et al., 2013). Terrestrial basalts from multiple settings shows a much more restricted range than lunar basalts (Prytulak et al., 2011, 2013, 2017; Wu et al., 2018). The measured V isotope range (∼2.3‰) of terrestrial magmatic rocks is displayed by the grey dashed line, with the heaviest V isotope samples thought to result from oxide fractionation (Prytulak et al., 2017). (For interpretation of the colours in the figure(s), the reader is referred to the web version of this article.)

interferences are resolved. Inter-laboratory comparison shows no resolvable differences in $\delta^{51}V$ for silicate rock reference materials (which generally have low S contents) at low- or medium-resolution MC-ICPMS (Nielsen et al., 2019). Despite the heavier, revised $\delta^{51}V$, chondrites are isotopically-lighter than BSE (Nielsen et al., 2019; Xue et al., 2018, Fig. 1). Nielsen et al. (2019) attributed this to nucleosynthetic-heterogeneity in the Solar System (demonstrated by correlations between chondrite class average $\delta^{51}V$ and $\varepsilon^{54}Cr$). Measurements of calcium–aluminium inclusions (CAIs) in CV chondrites show one subset (fine-grained CV3 CAIs) to have the lightest $\delta^{51}V$ measured thus far in the solar system ($\delta^{51}V_{AA} < -5.87‰$, Sossi et al., 2017, Fig. 1). These light $\delta^{51}V$ values have been attributed to ^{50}V production during intense early solar cosmic ray (SCR) irradiation, in agreement with mathematical predications for CAI formation close to an early, active Sun (Gounelle et al., 2001; Lee et al., 1998). This suggests cosmogenic reactions are viable mechanisms for production of light $\delta^{51}V$.

One body for which $\delta^{51}V$ data is lacking is the Moon. As a refractory element, V is expected to be isotopically-similar in the Moon and the Earth. Data from the Moon may also provide constraints on the origin of the difference in $\delta^{51}V$ observed between chondrites and the Earth.

2. Sampling approach

Nineteen unbrecciated lunar basalts from Apollo missions 11, 12, 14, 15, and 17 were selected based on geochemical and mineralogical variability (Table 1). Samples were processed in sufficient quantities for both V isotope and trace element measurements. The samples include both low-Ti and high-Ti basalts, with reported TiO_2 contents ranging from 2.2 wt% (15535) to 12.9 wt% (70215) (Table S7) and have reported modal ilmenite contents from 0.5% (12018) to 17% (70215, Table S5). An Apollo 11 Type A (high-K) basalt (10017), enriched in K, REEs and other incompatible trace elements (Tables S7, S9, Neal and Taylor, 1992), and a high-Al/low-K Apollo 14 basalt (14053) were included. Samples were extracted from the interior of their parents, with three exceptions. The exteriors of the parent samples 10017 and 12054 were sampled and a

fragment of a glass-splash coating from sample 12054 was also analysed. The glass was emplaced after a nearby impact or an eruptive event and has an Apollo 12 ilmenite basalt composition (similar to its host rock, Hartung et al., 1978). Interior aliquots of samples were obtained from a maximum depth of 2.5 cm within their parent samples (except 12063-343 which was located between 0.5–5 cm).

3. Methods

3.1. Sample preparation

Details of procedures for sample preparation, dissolution, ion-exchange chromatography and elemental and isotopic analyses can be found in the Supplementary Text. Briefly, sample chips were washed in ∼18.2 MΩ·cm ultra-pure water (MQ H_2O), centrifuged and dried at low temperature. Samples were crushed to homogenise any intra-sample geochemical variation using an agate pestle and mortar. Separate fractions of these powders were weighed for trace element determinations (∼10 mg) and vanadium isotope analyses (20–100 mg). Samples were digested in a multi-stage hotplate dissolution procedure.

3.2. Trace element analysis by ICPMS

Trace element analyses were performed using a *PerkinElmer®* *NexION®* 350D quadrupole ICPMS (at the Department of Earth Sciences, University of Oxford) on ×10000 dilutions of digested sample solutions. A Re-Rh-In internal standard addition (for monitoring instrumental drift) was performed using an in-line *ESI* prep-*FAST* auto-dilution system. The relative standard deviation was <5%, except for Li (7.9%). United States Geological Survey (USGS) reference material, BHVO-2, was measured alongside the lunar sample suite to assess accuracy.

3.3. Vanadium isotope analysis by MC-ICPMS

Chemical isolation of V was performed using methods outlined in Wu et al. (2016). Sample aliquots containing 5–10 μg of V

Table 1
$\delta^{51}V_{AA}$, selected element concentrations from ICPMS data, literature values for $^{158}Gd/^{157}Gd$, and sample exposure age.

Mission	Sample	Type	Sub-type	Location	$\delta^{51}V_{AA}$ (‰)	2s.d. (‰)	n	[V] (µg g^{-1})	TiO$_2$ (wt%)	^{158}Gd/ ^{157}Gd[a]	+/−	Exposure age (Ma)[b]
A11	10017-400	High-Ti/High-K	11A	exterior	−3.47	0.19	1	55	11.2	1.59726	0.00046	479 ± 60
	10017-405	High-Ti/High-K	11A	interior	−3.18	0.19	1	61	11.3			479 ± 60
	10020-255	High-Ti/Low-K	11B3	interior	−1.88	0.29	2	113	10.7			127 ± 25
	10044-655	High-Ti/Low-K	11B1	interior	−1.30	0.19	3	56	9.6	1.58681	0.00030	70 ± 17
A12	12018-598	Low-Ti Olivine		interior	−1.42	0.20	3	185	2.1	1.58924	0.00040	195 ± 16
	12054-13	Glass Splash			−1.63	0.21	4	168*	4.7*			–
	12054-146	Low-Ti Ilmenite Basalt		interior	−1.65	0.49	3	152	5.3			260 ± 70*
	12054-150	Low-Ti Ilmenite Basalt		exterior	−1.60	0.21	4	126	4.1			260 ± 70*
	12063-343	Low-Ti Ilmenite Basalt		interior	−1.35	0.21	3	188	4.9	1.58768	0.00016	95 ± 5
A14	14053-305	Low-Ti/High-Al/Low-K Basalt	HA	interior	−1.08	0.21	3	106	2.7			21 ± 5
A15	15016-240	Low-Ti Olivine-normative		interior	−1.53	0.21	2	224	2.1			322 ± 83
	15535-165	Low-Ti Olivine-normative		interior	−1.14	0.21	2	197	2.1			110 ± 20
	15556-258	Low-Ti Olivine-normative		interior	−2.00	0.42	2	227	2.4			546 ± 214
A17	70215-389	High Ti	17B2	interior	−1.31	0.21	2	167*	12.9*			126 ± 3
	70255-56	High Ti	17A	interior	−1.86	0.68	3	83	10.8			280 ± 85
	71135-34	High Ti	17B2	interior	−1.50	0.63	3	90	10.3			103 ± 3
	71546-22	High Ti	17A	interior	−1.24	0.49	2	120*	12.2*			110 ± 55*
	74275-355	High Ti	17C	interior	−1.00	0.19	3	131	12.4	1.58524	0.00001	32 ± 1
	75035-249	High Ti	Unclassified	interior	−1.71	0.19	2	31	10.5			77 ± 19
	Average High-Ti				*−1.85*	*1.66*						
	– excluding 10017				*−1.48*	*0.64*						
	Average Low-Ti				*−1.49*	*0.56*						

* Samples 12054-13, 70215-389, 71546-22 were not analysed for element concentrations by ICPMS in this study. An average of previously-reported elemental concentrations is used hereon (see Table S7). [a, b] Gd isotopes and exposure ages compiled from published values (Supplementary Text, Tables S3, S6). Exposure ages for 12054 (independently-calculated) and 71546 (estimated from other samples in the same rake) are less reliable than for the other samples in the suite (Section 4.5, Supplementary Text, Table S6).

were passed twice through cation-exchange columns (using *Bio-Rad*® AG50W-X12 200–400 mesh resin) to remove the majority of matrix elements (Fe, Ti, Al, Ca). An anion-exchange column (using *Bio-Rad*® AG1-X8 200–400 mesh resin) was then used to separate V from Cr, and repeated in scaled-down form to remove any remaining Cr.

Quantitative yield of V must be obtained to exclude possible isotopic fractionation during incomplete elution in ion-exchange chromatography. The yield was found to be 100 ± 15% at the end of the procedure (by comparing MC-ICPMS beam intensities to Quad ICP-MS measurements). Cuts were collected before and after the vanadium elution steps in the cation-exchange columns to ensure the calibration of V elution (Wu et al., 2016). Total V blanks were <0.3 ng, which is insignificant compared to the amount of V processed. Samples returned $^{49}Ti/^{51}V$ and $^{53}Cr/^{51}V$ ratios <0.00001 (Nielsen et al., 2011), confirming negligible contributions of ^{50}Cr and ^{50}Ti to the ^{50}V signal.

Vanadium isotopes were analysed on a *Plasma II* (*Nu Instruments*) MC-ICPMS in the MAGIC laboratories at the Department of Earth Sciences and Engineering, Imperial College London. Measurements were performed at solution concentrations of 600–800 ng g^{-1}. Samples were aspirated into a *Nu Instruments* DSN-100 to desolvate before injection into the plasma. Masses 49, 50, 51, 52 and 53 were monitored to measure V isotopes and to correct for Ti and Cr interferences on mass 50 (Table S1). Pseudo-high-resolution mode (M/ΔM > 5000) was used to resolve polyatomic interferences (particularly $^{40}Ar^{12}C^+$ from $^{52}Cr^+$) from the isotopes of interest. Faraday cups were equipped with 10^{11} Ω resistors, except for cups with low-intensity signals (m/z: 49, 50, 53), which were equipped with 10^{12} Ω resistors. This amplifies the resultant signal by a factor of 10 and improves signal/noise ratios. Each sample analysis was bracketed by two measurements of an Alfa Aesar (AA) V solution, and a well-characterised secondary standard from BDH chemicals (BDH, Nielsen et al., 2011). The AA standard defines zero (Section 1.4). BDH has been measured ($n = 1329$) to have a composition of $\delta^{51}V_{AA} = −1.17 ± 0.17$‰ (Prytulak et al., 2017). Measurements of BDH in this study gave an average $\delta^{51}V_{AA} = −1.21 ± 0.22$‰ ($n = 121$). United States

Geological Survey (USGS) reference materials BCR-2, BHVO-2, and BIR-1a were processed through the same ion-exchange procedures and $\delta^{51}V$ values were found to be in agreement with literature values (Table S2).

4. Results & discussion

4.1. Major and trace elements

Comparison of ICPMS elemental concentrations to previous analyses of lunar basalts shows that samples lie within expected ranges for their mare basalt subtype (Table 1, Figs. 3c, S2, S3). Sample sizes in this study are small (up to 125 mg) compared to the majority of literature chemical analyses (Table S7), which were typically performed on much larger aliquots (>1 g) and would be expected to be more representative of the geochemistry of parent samples (e.g. Ryder and Schuraytz, 2001). However, obtaining major and trace element concentrations and V isotope ratios on the same aliquots allows internally-consistent interpretation of isotopic variations. Major element concentrations of samples lie within 5% of published values, with minor exceptions. Samples 12018 (−9%), 12054-150 (+6.3%), and 70255 (−9.8%) show TiO$_2$ contents that differ by more than 5% from published values. Sample 12054-146 differs in K$_2$O by +8%, and sample 70255 differs in MnO by −6.3%. Chondrite-normalised REE patterns of the lunar samples match those of previous analyses and show the characteristic patterns expected for their sub-groups (Fig. S2). A detailed discussion of the trace element behaviour of the sample suite is beyond the scope of this study, however, elemental concentrations from this study and previously-reported values can be found in Tables S4, S7 & S9 and Supplementary Figs. S2 & S3.

4.2. Vanadium isotopes

Lunar basalts span a $\delta^{51}V$ range of ∼2.5‰, varying from $\delta^{51}V_{AA}$ = −3.47‰ (10017-400) to −1.00‰ (74275-355) (Table 1, Fig. 2). There is no systematic difference between $\delta^{51}V$ in high-Ti and low-Ti basalts (High-Ti: $\delta^{51}V_{AA}$ = −1.85 ± 1.66‰; Low-Ti: $\delta^{51}V_{AA}$ =
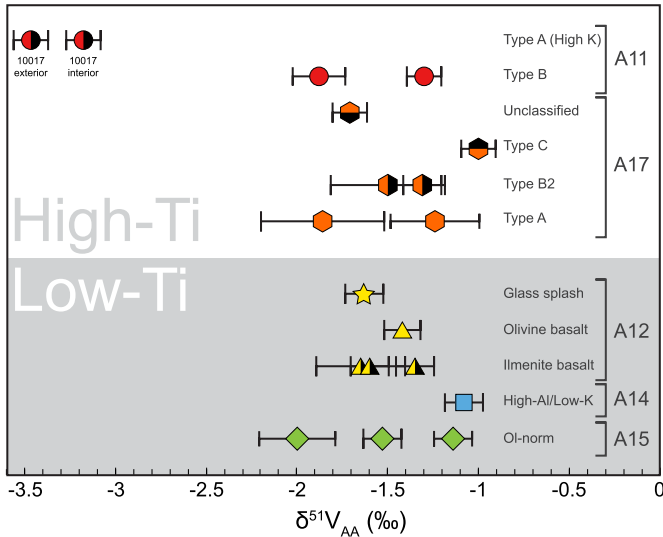
Fig. 2. $\delta^{51}V$ of the samples measured in this study. Samples are divided by high-Ti vs low-Ti type, mission, and sub-classification (Neal and Taylor, 1992). Aside from the two samples of 10017 (Apollo 11 Type A basalt), all chemical groups show an overlap in $\delta^{51}V$ between $\sim-2\permil$ to $\sim-1\permil$. Note in particular the range displayed by Apollo 15 olivine-normative basalts, despite their similarity in major and trace element compositions.

$-1.49 \pm 0.56\permil$, 2SD, Table 1, Figs. 2, 3a, b). Interior and exterior aliquots of Apollo 11 Type-A (high-K) basalt 10017 have the lightest isotopic compositions ($\delta^{51}V_{AA} = -3.18 \pm 0.19\permil$ and $-3.47 \pm 0.19\permil$, Fig. 2). Excluding these two samples reduces the lunar $\delta^{51}V$ range to $\sim1\permil$ and populations of high-Ti and low-Ti basalts are essentially indistinguishable (high-Ti basalt excl. 10017: $\delta^{51}V_{AA} = -1.48 \pm 0.64\permil$). The total lunar $\delta^{51}V$ range is larger than the total range of magmatic samples yet measured on the Earth ($\sim2.3\permil$, Fig. 1). Thirteen of the nineteen lunar basalts show $\delta^{51}V$ lighter than any terrestrial samples ($\delta^{51}V_{AA} < -1.32\permil$). Only three samples, 74275-355, 14053-305, and 15535-165 have isotopic compositions within the published range for terrestrial basalts ($\delta^{51}V_{AA} = -0.95 \pm 0.25\permil$ 2SD, Prytulak et al., 2013; Wu et al., 2018, Fig. 1).

4.3. Magmatic effects on V and $\delta^{51}V$

Under terrestrial magmatic conditions V behaves relatively incompatibly through magmatic evolution except during crystallisation of (Fe,Ti) oxides into which V^{3+} partitions readily (O'Neill and Navrotsky, 1984). On Earth, the most extreme $\delta^{51}V$ arises from $\sim$ closed system crystallisation of isotopically light (Fe, Ti) oxides, which drives residual melts to heavier compositions (up to $\delta^{51}V_{AA} \sim+1\permil$; Prytulak et al., 2017). Given the high modal proportions of (Fe,Ti) oxides (particularly ilmenite) in lunar basalts, it is tempting to assume that the large variability recorded in the lunar sample suite is a result of ilmenite–melt fractionation. However, oxygen fugacity is much lower on the Moon (IW-1 to IW-2) than in terrestrial melts, which not only affects the speciation and partitioning behaviour of V ($V^{3+} > V^{4+}$, on Earth $V^{4+} > V^{3+}$), but also the crystallising mineral phases (e.g. from lack of available Fe^{3+}). Analyses of minerals in lunar basalts show V present in spinel (<8000 ppm, Papike et al., 2005), armalcolite (<3000 ppm) and ilmenite (<2500 ppm, El Goresy et al., 1974), pyroxene (<500 ppm), and olivine (<80 ppm – Papike et al., 2005). Likewise, partition coefficients for V at low fO_2, show V to be compatible in spinel, armalcolite, ilmenite and pyroxene (in decreasing order of compatibility, Karner et al., 2006; Klemme et al., 2006; Papike et al., 2005). Under lunar conditions, V appears more compatible than in terrestrial settings. The abun-

dances of minerals in samples is highly-variable (Table S5) and crystal fractionation may control the observed range of $\delta^{51}V$.

Although V varies within the suite with varying major element compositions (Fig. 3c, Fig. S3) and mineralogy (e.g. ilmenite, pyroxene Fig. S4) there is no systematic relationship between $\delta^{51}V$ and TiO_2 or V (Fig. 3a, b) or between $\delta^{51}V$ and modal proportions of the major hosts for V (spinel, ilmenite, pyroxene, Fig. S4). Likewise, samples previously studied for mass-dependent isotopes (e.g. Cr, Fe, Fig. S5) do not show correlations with $\delta^{51}V$ (Bonnand et al., 2016; Liu et al., 2010; Sossi and Moynier, 2017; Wiesli et al., 2003). Apollo 11 Type-A basalt 10017 is $>1\permil$ lighter than the other basalts (Table 1, Fig. 2). Although the origin of the Apollo 11 Type-A basalts remains contested, the high-abundances of K, REEs, and other incompatible trace elements suggest involvement of a KREEP-like component (Neal and Taylor, 1992). The light $\delta^{51}V$ in this sample may reflect the extreme composition of this KREEP-y reservoir. However, KREEP is thought to represent the last vestiges of LMO prior to crystallisation. Prior removal of oxides from the LMO should leave this reservoir enriched in heavy $\delta^{51}V$ (i.e. opposite to the direction of $\delta^{51}V$ offset observed, assuming similar mineral–melt fractionations to terrestrial settings). The lack of evidence for systematic magmatic-driven $\delta^{51}V$ variability in this suite is further highlighted by the 0.84‰ isotopic difference between samples 15535 and 15556 (Fig. 2). These samples are genetically-related by olivine fractionation (Mason et al., 1972), which is unlikely to account for the large $\delta^{51}V$ difference observed.

4.4. Reduced magmatic $\delta^{51}V$ fractionation at lower fO_2

Considering the magnitude of isotopic fractionation associated with (Fe,Ti)oxide crystallisation on Earth (e.g. $\Delta^{51}V_{magnetite-melt} = -0.4$ to $-0.5\permil$ in Hekla and Anatahan lavas, Prytulak et al., 2017), the lack of correlation of $\delta^{51}V$ with TiO_2 or ilmenite or oxide content is notable, particularly since the range in abundances of (Fe,Ti) oxides in lunar basalts is much larger than in terrestrial samples. Wu et al. (2018) recently proposed a smaller terrestrial $\Delta^{51}V_{mineral-melt}$ of $-0.15\permil$. However, this factor was derived from a MORB-suite that is not cogenetic and has documented evidence of magma-mixing (indeed, their isotope-mixing calculations fit the $\delta^{51}V$ variation observed just as well as their reduced mineral–melt V isotope fractionation factor). A recent experimental study of V isotope fractionation between magnetite and hydrous granitic melt at $800\,°C$ and controlled fO_2 conditions (from FMQ-1 to FMQ+5) suggests $\Delta^{51}V_{magnetite-melt}$ reduces with decreasing fO_2 (Sossi et al., 2018). Extrapolating these results to lunar fO_2 and temperatures ($1/T^2$ dependence; Schauble, 2004) yields a $\Delta^{51}V_{oxide-melt}$ $\sim-0.2\permil$ (assuming lunar oxides fractionate $\delta^{51}V$ similarly to magnetite, which is not present at lunar fO_2). For lunar basalts, a reduced fractionation factor at lower fO_2 may explain a lack of variation between $\delta^{51}V$ and other geochemical parameters but cannot explain the wide range and light $\delta^{51}V$ of the suite.

4.5. Cosmogenic irradiation

Exposure ages have been previously-determined for most of the samples in this suite (Table 1, Table S6). To allow the most consistent cross-sample comparisons, exposure ages calculated using $^{81}Kr–Kr$ and ^{38}Ar (where $^{81}Kr–Kr$ data are absent) were chosen over other techniques due to their widespread adoption and inter-calibration (e.g. Hohenberg et al., 1978; see Supplementary Text, Table S6). The range of sample $\delta^{51}V$ is lighter and more variable at longer exposure ages (t_e, Fig. 4), implicating modification of primitive isotopic compositions by exposure-related processes.

Samples exposed at the lunar surface may be affected by meteorite sputtering, surficial contamination, solar wind implantation, or irradiation from high-energy particles derived from solar
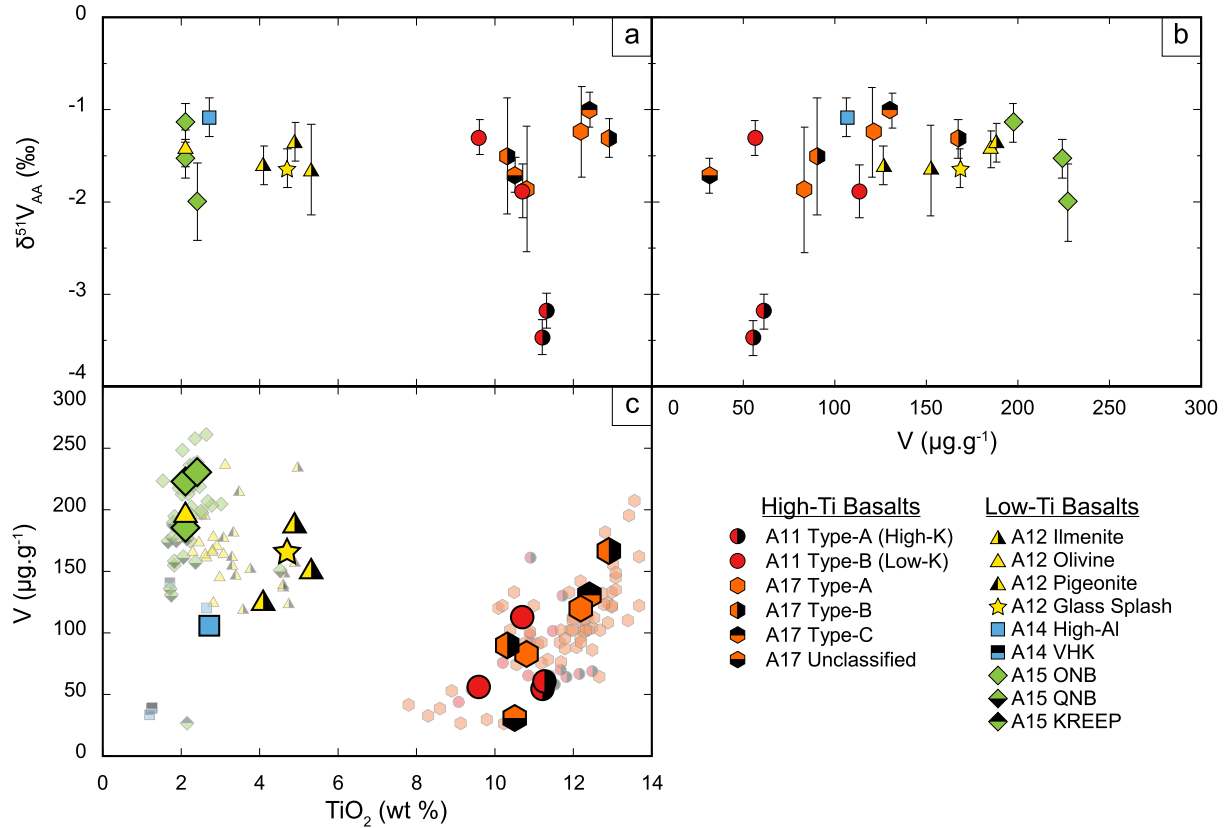
Fig. 3. Comparison of δ^{51}V, V and TiO_2 concentrations: a) δ^{51}V versus TiO_2 (wt%) contents; b) δ^{51}V versus V concentration; c) V concentration against TiO_2 concentration. Samples analysed in this study lie in the regions expected for their mare basalt subtype (c). A strong correlation exists between V and TiO_2 in the high-Ti basalts. Larger, solid symbols represent data from the samples in this study. Semi-transparent symbols are a compilation of literature-reported values for V and TiO_2 in lunar basalts (Table S8). There is no similar correlation between TiO_2 and δ^{51}V (a) or between V and δ^{51}V (b). Sample 10017 (two Apollo 11 high-K basalts) has δ^{51}V values which lie outside of the range of the other mare basalts.
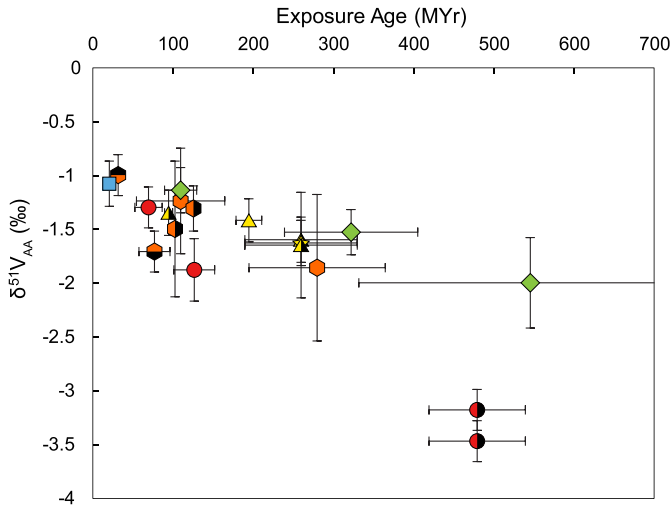

Fig. 4. Exposure age versus δ^{51}V. Samples with longer exposure ages have lighter V isotopic compositions. Details of sample exposure ages are outlined in the Supplementary Text and Table S6. Symbols as in Fig. 2.

and galactic cosmic rays (SCRs and GCRs). If exposure-related isotopic variability is achieved after crystallisation (as indicated by Fig. 4), sputtering, surficial contamination and solar wind implantation processes are unlikely to explain the observed δ^{51}V variability. All but three samples are picked from the interiors of their parents and would be shielded from these weakly-penetrating processes. Thus, cosmogenic irradiation from SCRs and GCRs is most

likely. Cosmogenic effects have been observed in lunar samples for neighbouring Ti and Cr isotope systems, with negative anomalies in ε^{50}Ti (Zhang et al., 2012) and positive anomalies in ε^{54}Cr and ε^{53}Cr (Mougel et al., 2018) attributed to neutron-capture processes. It is possible that similar processes operate on V isotopes.

The flux of energetic particles in SCRs and GCRs consists mainly of protons and alpha-particles (with minor fluxes of heavier nuclei). These primary particles can react with sample material to produce a cascade of secondary energetic particles (e.g. protons, neutrons, alpha-particles, ^{3}He, deuterium, muons, kaons, and pions) which can then further interact with sample material. Secondary neutrons are of particular interest for a number of elements, particularly those having isotopes with large neutron-capture cross-sections (e.g. gadolinium, Gd, where neutron-capture cross-sections for ^{157}Gd $\gg$ ^{156}Gd; Eugster et al., 1970). The ^{158}Gd/^{157}Gd ratio is sensitive to the flux of thermal neutrons generated during cosmic-ray reactions. Sample δ^{51}V shows a negative correlation with ^{158}Gd/^{157}Gd for five samples with published Gd isotope data (Fig. 5, Table S3), although the strength of this relationship may be enhanced by the position of sample 10017, which lies far outside the range of δ^{51}V and ^{158}Gd/^{157}Gd for the other samples. This correlation operates in a similar sense to that between δ^{51}V and exposure age (i.e. the most-exposed samples have the lightest δ^{51}V). However, three different samples (15016, 15556, 70215) have been measured for ε^{50}Ti (another neutron-capture-sensitive proxy, Zhang et al., 2012) and show similar trends (Fig. S6).
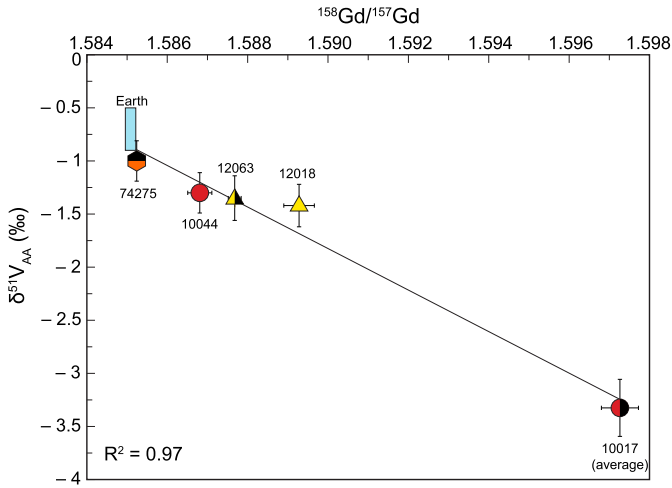
Fig. 5. Neutron-sensitive gadolinium isotope ratios versus δ^{51}V. The ratio of ^{158}Gd/^{157}Gd is a sensitive monitor of secondary neutrons produced during cosmic-ray bombardment of lunar material. Published ^{158}Gd/^{157}Gd for samples in this study linearly correlate with δ^{51}V. The internal and external aliquots of 10017 are averaged (for both δ^{51}V and ^{158}Gd/^{157}Gd) and plotted here as analyses were performed on different aliquots of this sample. The blue box represents the BSE estimate for δ^{51}V (Prytulak et al., 2013) and the terrestrial Gd isotope value from Dubois et al. (1992). A linear regression is calculated on the lunar samples. References for the Gd isotope data can be found in Table S3. Symbols as in Fig. 2.

4.6. Cross-sections

Earlier modelling of cosmogenic V isotope effects focused on production of ^{50}V from solar proton and He-nuclei interactions with CAI-precursor target materials (Gounelle et al., 2001; Lee et al., 1998). However, only a select handful of reaction pathways and target elements (Ti, Cr, and ^{51}V) were considered. Under lunar conditions, other target elements (e.g. Fe, Mn) may be important. Secondary particle fluxes (e.g. neutrons, Fig. 5, Fig. S6) are clearly present in these samples and should be considered. Cosmogenic reactions affecting ^{51}V must also be considered to ascertain the resultant effects on δ^{51}V.

Cross-sections for reactions involving the production or burnout of both ^{50}V and ^{51}V via proton-, alpha particle- and neutron-interactions with lunar sample compositions were calculated using TALYS-1.9 (Koning et al., 2008). This is the most recent iteration of the TALYS nuclear-modelling code and one of the most accurate codes for energies <200 MeV, being regularly evaluated and up-dated against experimental data. Although the energies of incident SCR and GCR particles regularly exceed this upper energy limit, this energy range should provide insights into both spallation- and capture-processes, and the relative importance of different target elements.

Cross-sections were calculated for nuclear reactions between target elements Ti, V, Cr, Mn and Fe (assumed to be present in natural isotope proportions) and incident neutrons (at energies 10^{-11} MeV–200 MeV), protons, and alpha-particles (energies 0.1 MeV–200 MeV). To allow comparison between the reactions ($n > 1000$), cross-section data was sub-divided into three categories: *burnout* of V isotopes (where target V isotope, j, forms another resulting element, R), *internal production* (target V isotope, i, produces the other V isotope, j – i.e. ^{50}V $\rightarrow$ ^{51}V or vice versa), and *external production* (where ^{nat}Ti, ^{nat}Cr, ^{nat}Mn, or ^{nat}Fe produces V isotope, j). All other factors being constant, *burnout* and *internal* production are controlled by the abundance of target V, and *external* production is controlled by the abundance of the non-V target element. The sums of the cross-sections, $\sum^j \sigma_{X,k}$, for *burnout*, *internal* and *external* production were calculated for each target, X, at different energies of incident particle, k (where k = proton, neutron, or alpha-particle; Fig. S10).

Reactions producing radioactive isotopes ^{51}Sc, ^{51}Ti, ^{51}Cr, ^{51}Mn, ^{51}Fe included in the sum of cross-sections for ^{51}V production (these isotopes are assumed to decay to before further interaction with energetic particles). Cross-sections for reaction pathways where the product nucleus is the same as the target nucleus (e.g. ^{50}V(n,n)^{50}V, or ^{51}V(p,n)^{51}Cr which decays to ^{51}V) were excluded.

The compiled cross-sections for each target ($\sum^j \sigma_{X,k}$) were adjusted to reflect atomic abundances of target elements relative to V in samples via:

$$\sum{}^j \sigma_{X,k,adjusted} = \sum{}^j \sigma_{X,k} \times [X]/[V] \tag{1}$$

where [X]/[V] is the ratio of target isotope or element relative to V. Total concentration-adjusted cross-sections ($\sum^j \sigma_{X,k,adjusted}$) of different particle pathways are compared for their effects on ^{50}V and ^{51}V (Fig. 6, where the "average" lunar sample composition is used).

Internal production displays lower cross-sections than external production in all scenarios, indicating that non-V target elements likely dominate cosmogenic production. Above ~50 MeV, Fe displays the largest cross-sections for production of both V isotopes in proton and alpha-particle reactions (Fig. 6b, c, e, f). Between 5–50 MeV, cross-sections for production of ^{50}V from protons with ^{nat}Ti (Fig. 6b) is higher than for production of ^{51}V (Fig. 6e). Burnout of either V isotope becomes increasingly-important at lower proton and alpha-particle energies (<5 MeV). At neutron energies >1 MeV, Cr and Fe appear to be most important for production of ^{51}V and ^{50}V (Fig. 6a, d). At neutron energies >50 MeV, Fe is the most important target element for production of either V isotope. Below 1 MeV, there are numerous pathways towards production of ^{51}V (via neutron interaction with Ti, Cr, ^{50}V), but no pathways for ^{50}V production. This has important implications: if thermal neutron capture is most significant amongst the array of possible reaction pathways, it is impossible to reconcile with the direction of cosmogenic isotope shift. Thus, charged-particle reactions or high-energy neutrons must contribute a significant amount to the total cosmogenic V production. In general, production cross-sections for ^{51}V appear larger than for ^{50}V (Fig. 7a, b, c) – however, a direct comparison must be carried out to ascertain the resulting effect on sample δ^{51}V.

4.7. Contribution to sample $\delta^{51}V$

The total ^{51}V/^{50}V in irradiated samples can be displayed as follows:

$$\left(\frac{n(^{51}\text{V})}{n(^{50}\text{V})}\right)_{final} = \frac{[n(^{51}\text{V})_0 + n(^{51}\text{V})_{cosm}]}{[n(^{50}\text{V})_0 + n(^{50}\text{V})_{cosm}]} \tag{2}$$

where $n(^jV)_0$ is the initial number of atoms of isotope, j, and $n(^jV)_{cosm}$ is the number of atoms of isotope, j (i.e. ^{51}V, ^{50}V), produced through cosmogenic reactions:
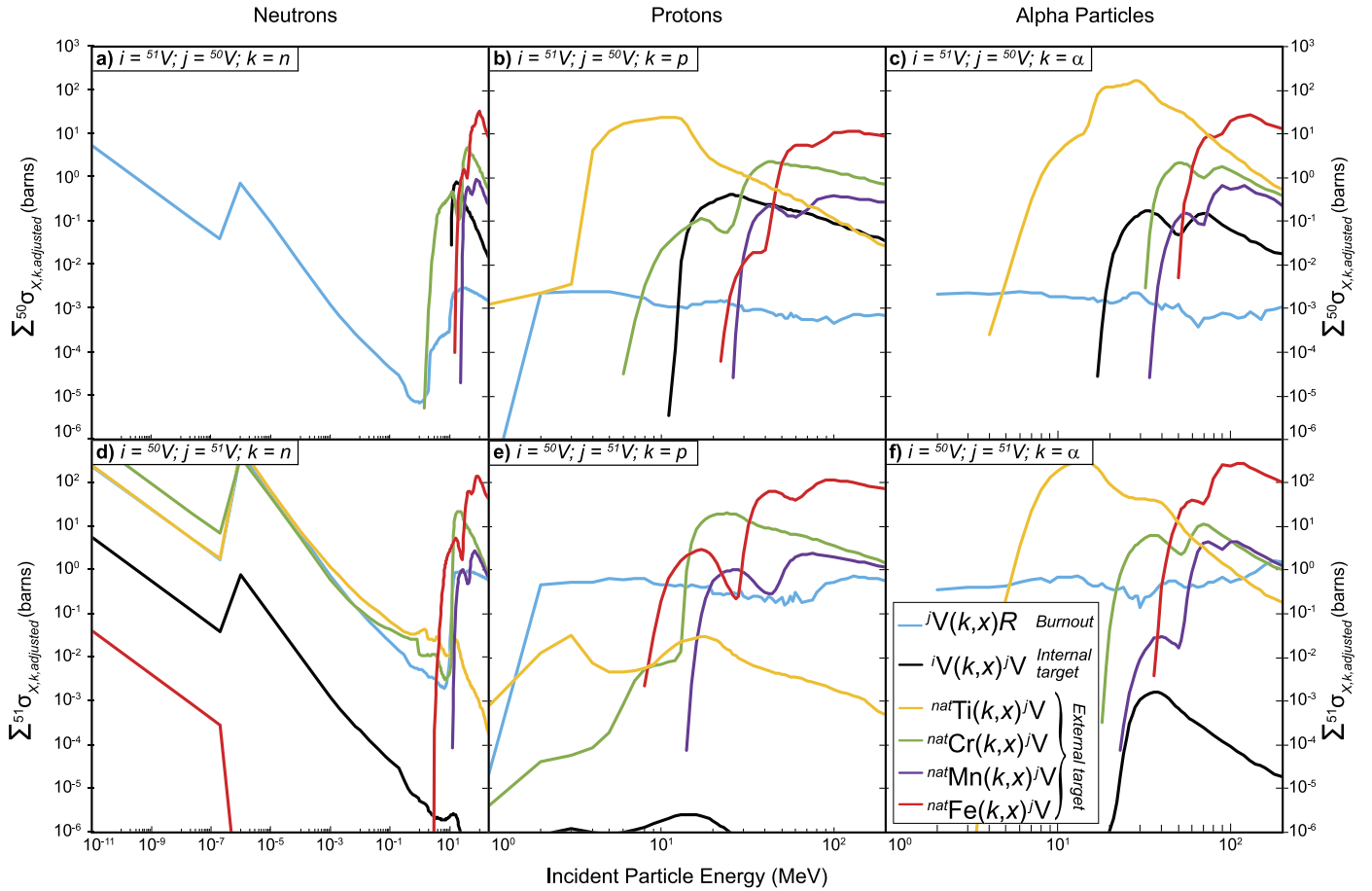
$$n(^jV)_{cosm} = n(^jV)_{external} + n(^jV)_{internal} - n(^jV)_{burnout} \tag{3}$$

The resulting isotopic effect is:

$$\Delta^{51}V_{cosm} = \left[\frac{\frac{n(^{51}V_{final})}{n(^{50}V_{final})}}{\frac{n(^{51}V_0)}{n(^{50}V_0)}} - 1\right] \times 1000 \tag{4}$$

Assuming a natural isotopic ratio ($\frac{n(^{51}V_0)}{n(^{50}V_0)} = 400$) substituting for the terms in Equation (2) gives:

$$\Delta^{51}V_{cosm} = \left[\frac{n(^{51}V_{cosm}) - n(^{50}V_{cosm}) \times 400}{n(^{50}V_{cosm}) + n(^{51}V_0)}\right] \times 1000 \tag{5}$$

Fig. 6. The sum of adjusted cross-sections ($\sum {}^j\sigma_{X,k}$, y-axes) for reactions between an incident particle, k, (k = neutron, proton or alpha particle) and nuclei (X) to either produce or burn out ${}^jV$ (where j is the V-isotope of interest – i.e. ${}^{50}V$, ${}^{51}V$) at different particle energies (x-axis). Reactions are broken down into three categories: burnout (light blue) of ${}^jV$ to another isotope, R; internal production (black) of ${}^jV$ from ${}^iV$ (j = 50, 51; i = 51, 50); external production of ${}^jV$ from target elements ${}^{nat}Ti$ (gold); ${}^{nat}Cr$ (green); ${}^{nat}Mn$ (purple); ${}^{nat}Fe$ (red). Cross-sections are adjusted to the average composition of the suite via [X]/[V] (where [X] is the atomic abundance of the target element or isotope, [V] is the atomic abundance of V). Targets are assumed to have natural isotopic abundances. Cross-section curves are displayed for each incident particle (neutrons a, d; protons b, e; alpha-particles c, f) and its effect on each isotope of V (${}^{50}V$: a, b, c; ${}^{51}V$: d, e, f). Within each panel, the curves represent reactions which add to the abundance of isotope ${}^jV$, except the burnout curves (light blue) which will decrease the abundance of ${}^jV$. Note the different energy scales for neutrons and protons/alpha-particles.

Thus, for a resulting cosmogenic isotopic shift ($\Delta^{51}V_{cosm}$) of 0‰:

$$n\left({}^{51}V_{cosm}\right) = n\left({}^{50}V_{cosm}\right) \times 400 \qquad (6)$$

The production of cosmogenic ${}^{51}V$ and ${}^{50}V$ is proportional to the sum (i.e. *internal + external − burnout*) of their concentration-adjusted cross-sections ($\sum {}^j\sigma_{total\text{-}adjusted}$). Assuming $[V]_0 \gg [V]_{cosm}$, if $\sum {}^{51}\sigma_{total\text{-}adjusted} > (\sum {}^{50}\sigma_{total\text{-}adjusted} \times 400)$ the resulting isotope ratio will increase and if $\sum {}^{51}\sigma_{total\text{-}adjusted} < (\sum {}^{50}\sigma_{total\text{-}adjusted} \times 400)$ the resulting isotope ratio will decrease. For ease of comparison between the total adjusted cross-sections a new variable, the "excess total ${}^{51}V$ cross-section" is defined:

$$\varepsilon^{51}\sigma_{total} = \left(\sum {}^{51}\sigma_{total\text{-}adjusted} - \sum {}^{50}\sigma_{total\text{-}adjusted} \times 400\right)/\left[{}^{51}V\right] \qquad (7)$$

This is more useful than a direct cross-section ratio ($\sum {}^{51}\sigma_{total\text{-}adjusted}/\sum {}^{50}\sigma_{total\text{-}adjusted}$) since it allows direct inspection of the isotopic effects of particular pathways at different energies and can account for instances where the sum of concentration-adjusted cross-sections for an isotope is ≤ 0 (e.g. where burnout is more significant than production).

For all the particle reactions considered, it appears that only neutron capture ($< 1 \times 10^{-3}$ MeV) can produce excesses in $\varepsilon^{51}\sigma_{total}$ (Fig. 7d, g). There are negative excursions in $\varepsilon^{51}\sigma_X$ for

proton and alpha-particle reactions with Ti between 20–100 MeV (Fig. 7e, f), and smaller negative excursions in $\varepsilon^{51}\sigma_{total}$ for Fe reactions with protons >50 MeV. Similarly, high-energy neutrons display negative $\varepsilon^{51}\sigma_X$ for Fe (>10 MeV, Fig. 7d). The magnitude of the cosmogenic isotope effect is expected to vary with sample compositions (i.e. changing [X]/[V] ratio, Fig. 7g, h, i). High-Ti samples are expected to show a stronger $\varepsilon^{51}\sigma$ response to interactions with protons and alpha-particles when compared to average sample or low-Ti sample compositions. However, at lower neutron energies ($<10^{-3}$ MeV), high-Ti samples would be expected to display isotopically-heavier cosmogenic signatures when compared to low-Ti samples (Fig. 7g). It appears that for protons and alpha-particles, Fe and Ti are the primary contributors to V isotope anomalies for the energy ranges investigated. Burnout of V and internal production are relatively unimportant in affecting the final isotopic ratio.

4.8. Reconciling with chemical compositions

Plotting sample $\delta^{51}V$ against exposure age over V concentration ($t_e/[V]$) yields a strong linear correlation (Fig. 8a). This correlation is stronger than the relationship between $\delta^{51}V$ and $t_e*[Ti]/[V]$ (and $t_e*[Cr]/[V]$, Fig. S7), and similar to the correlation between $\delta^{51}V$ and $t_e*[Fe]/[V]$ (Fig. 8b) and $t_e*[Mn]/[V]$ (Fig. S7). The strong correlation between $\delta^{51}V$ and $t_e/[V]$ suggests the concentration of [V] (assuming $[V]_0 \gg [V]_{cosm}$) in samples is more
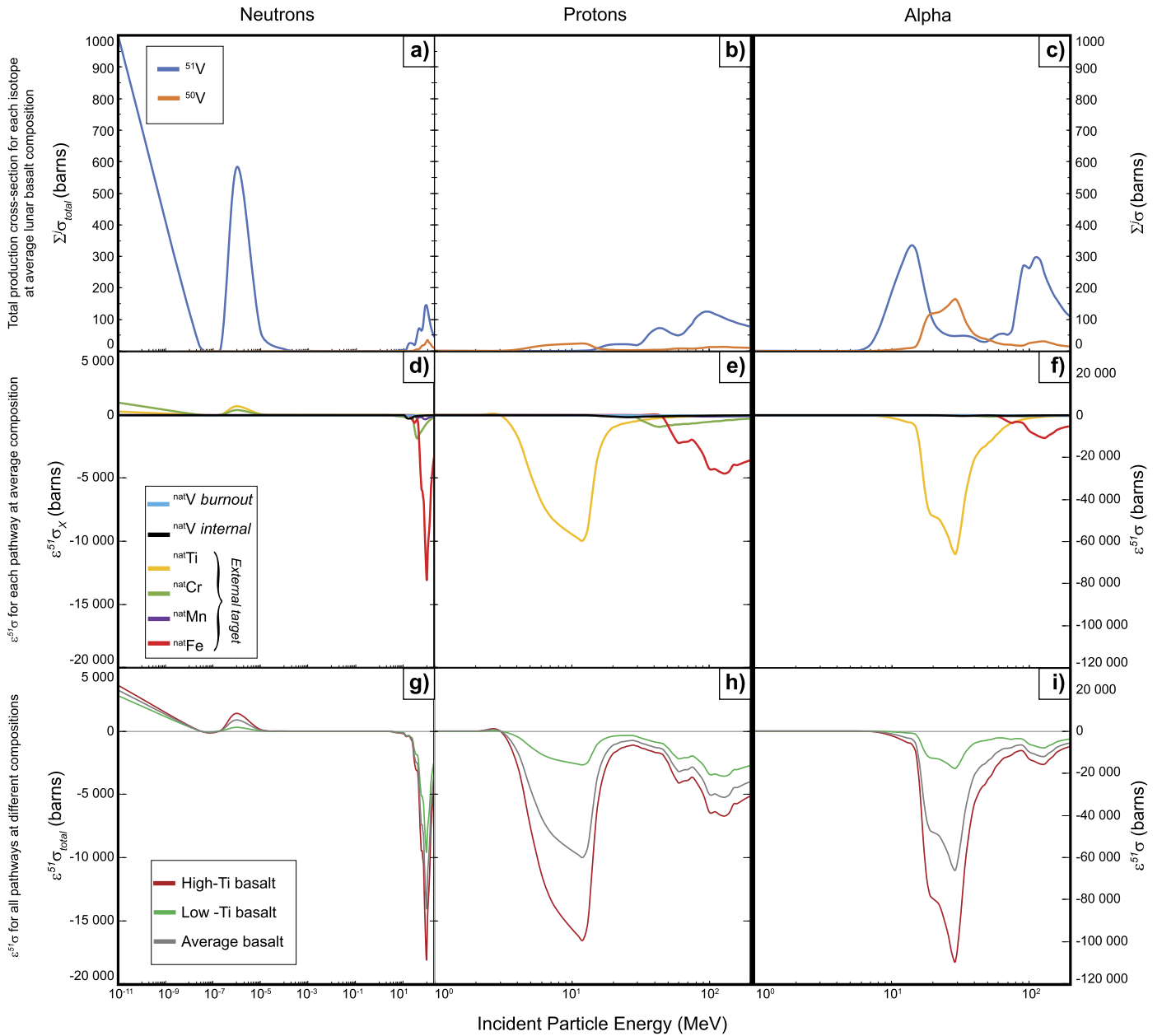
Fig. 7. The resulting isotopic effects of cosmogenic reactions between neutrons, protons, and alpha-particles and lunar basalt compositions at different energies. The total concentration-adjusted cross-sections affecting ^{50}V and ^{51}V from interactions between neutrons (a), protons (b), and alpha-particles (c) and targets of average lunar basalt composition at different energies are displayed. Cross-sections for production of ^{51}V is higher than ^{50}V, except for alpha-particle reactions between 20–50 MeV. The excess ^{51}V production cross-section for different target elements ($\varepsilon^{51}\sigma_X$, see Section 4.7) varies across the range of incident particle energies and particle compositions (d, e, f). The total excess ^{51}V production cross-section ($\varepsilon^{51}\sigma_{total}$) changes in intensity with changing target chemical compositions (g, h, i). For all particles (except neutrons below 10^{-5} MeV) there are significant negative $\varepsilon^{51}\sigma$ deviations. Thermal neutrons ($\leq 2.5 \times 10^{-8}$ MeV) show positive $\varepsilon^{51}\sigma$ deviations (**g**), as only ^{51}V production is viable the target elements investigated (Fig. 6a, 6d). Average and low-Ti basalts show reduced $\varepsilon^{51}\sigma_{total}$ deviations compared to high-Ti basalts reflecting variation in [X]/[V] between samples. At high-energies (>50 MeV) negative deviations in $\varepsilon^{51}\sigma$ are seen from the effect of Fe as a target. Key displayed in a), d), g).

important in controlling the resultant $\delta^{51}V$ after cosmogenic exposure than the concentration of the target element – i.e. the target element concentration doesn't vary much compared to [V]. Both Mn and Fe are relatively restricted in variability compared to V, Cr, and Ti (Table S4, S7). However, the concentration-adjusted cross-sections for Mn are orders of magnitude lower than for Fe (Fig. 6), and Fe is therefore more likely to be the primary target element. Iron is relatively invariable within this suite (RSD ~8%). A lone high-energy (600 MeV and 21 GeV) experimental-study of V-production from proton-induced Fe-spallation (Perron, 1976) indicates that production cross-sections are still significant at high-energies, and the ratio of $^{51}V/^{50}V$ produced is low (<1,

and this ratio is lower at higher proton energies). Thus, Fe appears to remain an important target for production of light $\delta^{51}V$ for higher-energies particle fluxes (e.g. as seen in GCRs) than directly calculated here.

The weaker correlation with $t_e \times$ [Ti]/[V] (despite strong $\varepsilon^{51}\sigma$ depletion at certain energy intervals, Fig. 7e, f) could be due to a number of reasons: 1) the real energetic particle flux is stronger for parts of the energy spectrum where cross-sections with Fe are strongest (typically energies >50 MeV), or 2) thermal neutron capture on Ti at low energies is quantitatively-important – the production of ^{51}V here would counteract production of lower $^{51}V/^{50}V$ from Ti reactions and protons/alpha-particles.
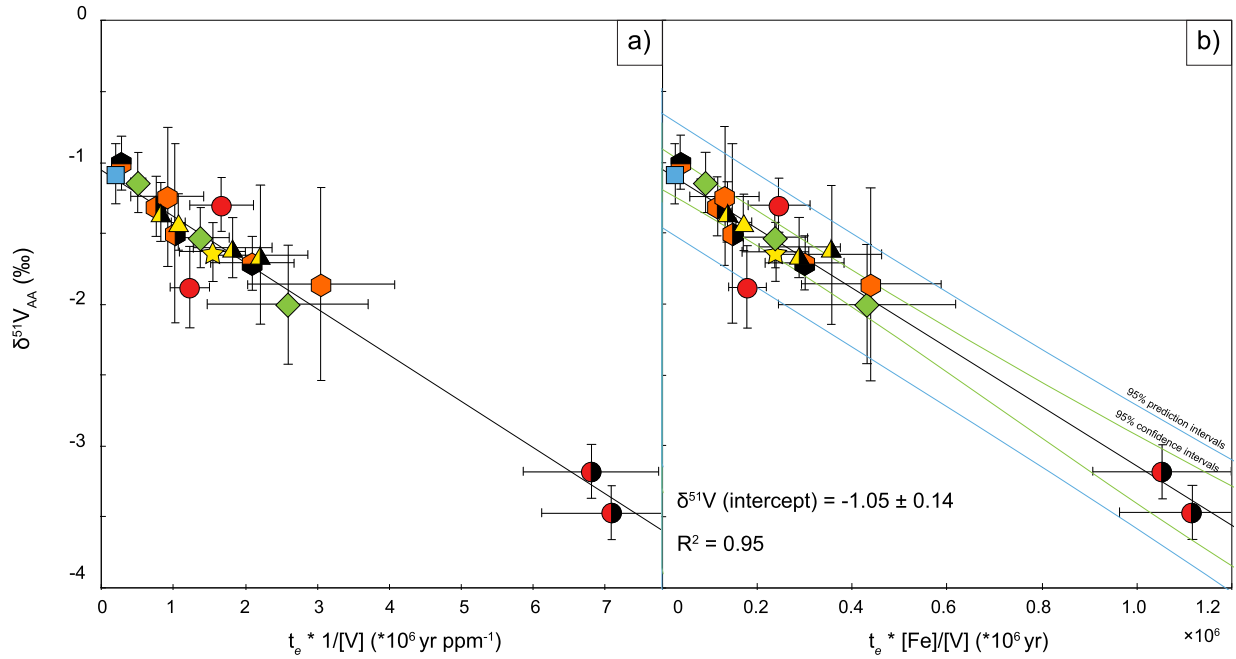
Fig. 8. Sample δ^{51}V versus $t_e \times 1/[V]$ and $t_e \times [Fe]/[V]$. Strong correlations between δ^{51}V and $t_e \times 1/[V]$ (a) indicate that the important targets for isotopic effects are relatively invariant in abundance in the samples. The most likely target element of importance is Fe (b) due to its high-concentration within the samples, relative invariance in concentration, high cross-sections (especially >50 MeV) and negative $\varepsilon^{51}\sigma$ deviations (where cosmogenic reactions will shift δ^{51}V to lighter values). Correlations between δ^{51}V and $t_e \times 1/[V]$ and $t_e \times [Fe]/[V]$ are stronger than those for Ti, Cr and Mn (Fig. S7). The fact that most samples fall on the same trendline indicates that pre-irradiation δ^{51}V variation is restricted, despite highly-variable magmatic histories. A linear regression ($R^2 = 0.95$) is calculated to intercept at δ^{51}V $= -1.05 \pm 0.14$ (95% confidence intervals). Samples with only literature chemical compositions available (Table 1) or estimated exposure ages (12054-13, 12054-146, 12054-150, 70215-389, 71546-22) were excluded from regression calculations, but included in the calculation of R^2 (excluding literature samples: slope $= -2.0911$, intercept $= -1.054$, $R^2 = 0.9500$; including all samples: slope $= -2.0915$, intercept $= -1.043$, $R^2 = 0.9477$). Symbols same as Figs. 2, 3, 4, 5.

In summary, thermal neutrons – although clearly present in sufficient fluxes to impart significant ^{158}Gd/^{157}Gd excesses (Fig. 5) and ε^{50}Ti depletions (Fig. S6) – cannot be the sole cause of δ^{51}V alteration due the lack of viable pathways for neutron capture production of ^{50}V (Fig. 6). Significant fluxes of higher-energy neutrons (>1 MeV, Fig. 7d, f), protons, or alpha-particles (>5 MeV) must have been present in the samples during their periods of exposure at the lunar surface. The most plausible target element is Fe (Fig. 8a, b). Although SCRs have significantly weaker penetrative-ability than GCRs, both processes may be important for these samples obtained from shallow depths (Section 2).

4.9. Pre-irradiation compositions and implications for the solar system

A linear regression is calculated on the data in Fig. 8b yielding a slope of -2.091×10^{-6}, and a y-intercept of -1.05 ($R^2 = 0.95$). Samples with less-reliable exposure ages (12054, 71546, Supplementary Text, Table S6) or where only literature chemical data exists (12054-13, 70215, 71546) were excluded from this calculation, but their inclusion only slightly affects the resulting regression (slope $= -2.092 \times 10^{-6}$, $R^2 = 0.95$). The coincidence of high-Ti and low-Ti basalts upon the same regression line indicates that, despite different mantle sources and magmatic histories, high-Ti and low-Ti basalts have similar pre-exposure δ^{51}V. The two samples with the shortest exposure age (14053-305, 74275-355) have similar δ^{51}V values despite their significant geochemical differences. Exclusion of the unusually-light sample, 10017, (Section 4.3) results in a similar regression with slope -1.989×10^{-6} and intercept -1.06. Thus, the δ^{51}V range across all samples can largely be attributed to cosmogenic processes post-crystallisation. The intercept of Fig. 8b defines the pre-irradiation average δ^{51}V for the suite. Pre-irradiation lunar basalt composition is estimated to be δ^{51}V$_{AA}$ $= -1.05 \pm 0.14‰$ (95% CI). Although fractionation during partial melting cannot be excluded, and so an estimate of the bulk lunar

mantle δ^{51}V cannot be confidently made, the convergence of high-Ti and low-Ti suites suggests δ^{51}V may be relatively uniform in the basalt source regions.

Recent work by Nielsen et al. (2019) and Xue et al. (2018) using higher-resolution MC-ICPMS shows chondrites to have a restricted range in isotopic compositions (Section 1.4). For chondrites with published noble gas data, cosmogenic exposure ages (using Ne isotopes following Scherer et al., 1998, Table S10) vary between 0.3 and 33.1 Ma. This is shorter than most of the lunar basalts in this study. Plotting meteorite sample δ^{51}V against $t_e * [Fe]/[V]$ shows meteorites to lie on the same trend as lunar samples (within analytical error, Fig. 9). Linear regression shows meteorites to intercept at δ^{51}V$_{AA} = -1.06 \pm 0.06‰$ (95% CI). Thus, it appears that recent cosmogenic exposure can explain δ^{51}V variations in chondrites in Nielsen et al. (2019). This is not related to differential incorporation of irradiated components (e.g. CAIs), but to irradiation processes operating after the breakup of meteorite parent bodies. The δ^{51}V variability seen in chondrites is unlikely to be related to nucleosynthetic heterogeneities: ordinary chondrites show ε^{54}Cr deficits relative to carbonaceous chondrites (Qin et al., 2010), but variable δ^{51}V (Nielsen et al., 2019; Xue et al., 2018). In summary, not only do lunar samples and chondrites show small pre-irradiation δ^{51}V variability within their own suites, but the Moon and chondrites have similar pre-irradiation values.

Early studies of V isotope ratios in geological materials (prior to the development of MC-ICPMS) were hindered by relatively poor analytical precision, but studies of iron meteorites (e.g. Stauffer and Honda, 1961) reported samples with remarkable ^{51}V/^{50}V ratios (ranging from ~ 5 to 150). In light of the relationship between δ^{51}V and $t_e * [Fe]/[V]$ seen in lunar samples and chondrites, and the apparent importance of Fe as a target element, these extreme ratios appear to be in accordance with the chemical compositions of iron meteorites where [V] typically is <1 ppm.
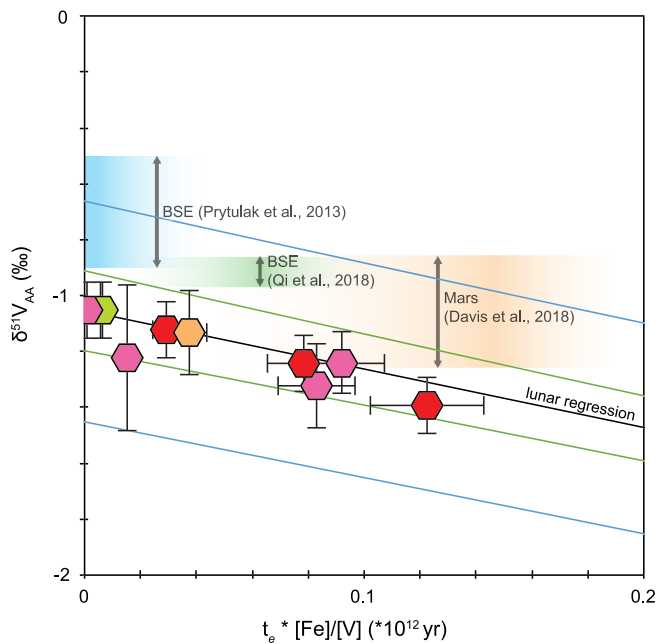
Fig. 9. Chondrite $\delta^{51}V$ versus $t_e \times$ [Fe]/[V]. Samples with available exposure age, chemical and $\delta^{51}V$ data (from Nielsen et al., 2019) fall on the linear regression calculated for lunar samples (within analytical error, Fig. 8b), strongly suggesting the variation observed in recent chondrite data (Nielsen et al., 2019; Xue et al., 2018) is also due to irradiation of samples. Pre-irradiation values overlap with estimates for the BSE (Prytulak et al., 2013; Qi et al., 2018) and Mars (Davis et al., 2018) suggesting that $\delta^{51}V$ is relatively uniform between planetary and chondrite parent bodies measured thus far. Symbols as in Fig. 1 (carbonaceous chondrites: pink; ordinary chondrites: red; enstatite chondrite: green; Rumuruti-chondrite: yellow). Data displayed in Table S10.

The pre-irradiation $\delta^{51}V$ calculated for the Moon ($\delta^{51}V_{AA} = -1.05 \pm 0.14\%$, 95% CI) is in accordance with the value obtained for chondrites ($\delta^{51}V_{AA} = -1.06 \pm 0.06\%$, 95% CI) and Mars ($\delta^{51}V_{AA} = -1.05 \pm 0.20\%$, 2SD, Davis et al., 2018). These values are similar to the composition of BSE ($\delta^{51}V_{AA} = -0.7 \pm 0.2\%$) from Prytulak et al. (2013) and largely overlap with a more recent estimate from Qi et al. (2018) ($\delta^{51}V_{AA} = -0.91 \pm 0.05$, 2SD, Fig. 9). In contrast to initial studies (Nielsen et al., 2014) it appears that the $\delta^{51}V$ of planetary bodies (Earth, Moon, Mars) and chondrites are remarkably similar.

5. Conclusions

1. Vanadium is more compatible during melting, and has higher partition coefficients in crystallising mineral phases, on the Moon compared to the Earth. Therefore, multiple phases can host V in significant quantities during lunar fractional crystallisation.
2. There is no correlation between sample $\delta^{51}V$ and mineralogy or chemical composition. High-Ti (excluding 10017) and low-Ti basalts span a similar range in $\delta^{51}V$. Lunar basalts are mostly isotopically lighter than terrestrial basalts, but also show a high degree of variability, spanning a range equal to the most extreme products of magmatic differentiation processes on Earth (Prytulak et al., 2017).
3. Terrestrial crystallisation of (Fe, Ti) oxides strongly fractionates V isotopes, but despite large variations in oxide content in the lunar suite, there is little evidence for oxide crystallisation controlling $\delta^{51}V$. Recent experiments demonstrate $\Delta^{51}V_{magnetite-melt}$ decreases with progressively reducing conditions (Sossi et al., 2018). Thus, it is possible that reduced lunar fO_2 could render $\Delta^{51}V_{oxide-melt}$ analytically-insignificant.

4. Vanadium isotopes correlate with exposure age and neutron-sensitive Gd isotopes, with longer-exposed samples having lighter $\delta^{51}V$ (Fig. 4). Calculations of reaction cross-sections protons, alpha-particles and neutrons indicate that Ti and Fe are most important potential targets for cosmogenic alteration of $\delta^{51}V$. However, neutron-capture alone cannot drive the isotopic variability observed.
5. The correlation observed between $\delta^{51}V$ and t_e* [Fe]/[V] suggests Fe is the primary target element of importance for cosmogenic V isotope effects, and similar pre-exposure $\delta^{51}V$ for high-Ti and low-Ti basalts ($\delta^{51}V_{AA} = -1.05 \pm 0.14\%$, 95% CI, Fig. 8b). The similarity in V isotope ratios between lunar basalts and the BSE adds further weight to the growing body of evidence that the Moon is the Earth's isotopic twin.
6. The co-linearity of the lunar and meteorite correlations for V isotopes versus t_e* [Fe]/[V] implies cosmogenic effects as the dominant cause of solar system V isotope variability. There is no longer evidence for a significant difference between the BSE and other reservoirs.
7. The magnitude of cosmogenic isotope effects seen in vanadium isotope ratios is much larger than those seen in Cr and Ti isotopes. Vanadium isotopes therefore have the potential to be a useful proxy for recording exposure histories in extra-terrestrial materials.

Appendix A. Supplementary material

Supplementary material related to this article can be found online at https://doi.org/10.1016/j.epsl.2019.01.008.

References

Akram, W., Schonbachler, M., 2016. Zirconium isotope constraints on the composition of Theia and current Moon-forming theories. Earth Planet. Sci. Lett. 449, 302–310.

Armytage, R.M.G., Georg, R.B., Williams, H.M., Halliday, A.N., 2012. Silicon isotopes in lunar rocks: implications for the Moon's formation and the early history of the Earth. Geochim. Cosmochim. Acta 77, 504–514.

Bonnand, P., Parkinson, I.J., Anand, M., 2016. Mass dependent fractionation of stable chromium isotopes in mare basalts: implications for the formation and the differentiation of the Moon. Geochim. Cosmochim. Acta 175, 208–221.

Cameron, A.G.W., Ward, W.R., 1976. The origin of the Moon. In: Abstracts of the Lunar and Planetary Science Conference 7, p. 120.

Canil, D., 1997. Vanadium partitioning and the oxidation state of Archaean komatiite magmas. Nature 389, 842–845.

Canup, R.M., 2004. Simulations of a late lunar-forming impact. Icarus 168, 433–456.

Canup, R.M., 2012. Forming a Moon with an Earth-like composition via a Giant Impact. Science 338, 1052–1055.

Cuk, M., Stewart, S.T., 2012. Making the Moon from a fast-spinning Earth: a giant impact followed by resonant despinning. Science 338, 1047–1052.

Dauphas, N., Burkhardt, C., Warren, P.H., Fang-Zhen, T., 2014. Geochemical arguments for an Earth-like Moon-forming impactor. Philos. Trans. R. Soc. A, Math. Phys. Eng. Sci. 372, 20130244.

Davis, D.M., Nielsen, S.G., Magna, T., Mezger, K., 2018. Constraints on the vanadium isotope composition of Mars. In: LPSC 49th Abstr., p. 1696.

Dubois, J.C., Retali, G., Cesario, J., 1992. Isotopic analysis of rare earth elements by total vaporization of samples in thermal ionization mass spectrometry. Int. J. Mass Spectrom. Ion Process. 120, 163–177.

El Goresy, A., Ramdohr, P., Medenbach, O., Bernhardt, H.J., 1974. Taurus–Littrow TiO$_2$-rich basalts: opaque mineralogy and geochemistry. In: Proceedings of the 5th Lunar Science Conference, vol. 1. Houston, Tex., March 18–22, 1974. Pergamon Press, Inc., New York, pp. 627–652.

Elkins-Tanton, L.T., Burgess, S., Yin, Q.Z., 2011. The lunar magma ocean: reconciling the solidification process with lunar petrology and geochronology. Earth Planet. Sci. Lett. 304, 326–336.

Eugster, O., Tera, F., Burnett, D.S., Wasserburg, G.J., 1970. Isotopic composition of Gd and neutron capture effects in samples from Apollo-11. Earth Planet. Sci. Lett. 8, 20.

Goderis, S., Chakrabarti, R., Debaille, V., Kodolanyi, J., 2016. Isotopes in cosmochemistry: recipe for a Solar System. J. Anal. At. Spectrom. 31, 841–862.

Gounelle, M., Shu, F.H., Shang, H., Glassgold, A.E., Rehm, K.E., Lee, T., 2001. Extinct radioactivities and protosolar cosmic rays: self-shielding and light elements. Astrophys. J. 548, 1051–1070.

Hartmann, W.K., Davis, D.R., 1975. Satellite-sized planetesimals and lunar origin. Icarus 24, 504–515.

Hartung, J.B., Hauser, E.E., Horz, F., Morrison, D.A., Schonfeld, E., Zook, H.A., Mandeville, J.-C., McDonnell, J.A.M., Schaal, R.B., Zinner, E., 1978. Lunar surface processes – report of the 12054 consortium. In: Lunar and Planetary Science Conference Proceedings, pp. 2507–2537.

Hohenberg, C.M., Marti, K., Podosek, F.A., Reedy, R.A., Shirk, J.R., 1978. Comparisons between observed and predicted cosmogenic noble gases in lunar samples. In: Proc. Lunar Planet. Sci. Conf., vol. 9, pp. 2311–2344.

Karner, J., Papike, J.J., Shearer, C.K., 2006. Comparative planetary mineralogy: pyroxene major- and minor-element chemistry and partitioning of vanadium between pyroxene and melt in planetary basalts. Am. Mineral. 91, 1574–1582.S.

Klemme, S., Gunther, D., Hametner, K., Prowatke, S., Zack, T., 2006. The partitioning of trace elements between ilmenite, ulvospinel, annalcolite and silicate melts with implications for the early differentiation of the moon. Chem. Geol. 234, 251–263.

Koning, A.J., Hilaire, S., Duijvestijn, M.C., 2008. TALYS-1.0. In: Bersillon, O., Gunsing, F., Bauge, E., Jacqmin, R., Leray, S. (Eds.), Proceedings of the International Conference on Nuclear Data for Science and Technology. April 22–27, 2007, Nice, France. EDP Sciences, pp. 211–214.

Kruijer, T.S., Kleine, T., Fischer-Gödde, M., Sprung, P., 2015. Lunar tungsten isotopic evidence for the late veneer. Nature 520, 534.

Lee, C.-T.A., Brandon, A.D., Norman, M., 2003. Vanadium in peridotites as a proxy for paleo-fO_2 during partial melting: prospects, limitations, and implications. Geochim. Cosmochim. Acta 67, 3045–3064.

Lee, C.-T.A., Leeman, W.P., Canil, D., Li, Z.-X.A., 2005. Similar V/Sc systematics in MORB and arc basalts: implications for the oxygen fugacities of their mantle source regions. J. Petrol. 46, 2313–2336.

Lee, T., Shu, F.H., Shang, H., Glassgold, A.E., Rehm, K.E., 1998. Protostellar cosmic rays and extinct radioactivities in meteorites. Astrophys. J. 506, 898–912.

Li, Z.-X.A., Lee, C.-T.A., 2004. The constancy of upper mantle fO_2 through time inferred from V/Sc ratios in basalts. Earth Planet. Sci. Lett. 228, 483–493.

Liu, Y., Spicuzza, M.J., Craddock, P.R., Day, J.M.D., Valley, J.W., Dauphas, N., Taylor, L.A., 2010. Oxygen and iron isotope constraints on near-surface fractionation effects and the composition of lunar mare basalt source regions. Geochim. Cosmochim. Acta 74, 6249–6262.

Lugmair, G.W., Shukolyukov, A., 1998. Early solar system timescales according to Mn-53–Cr-53 systematics. Geochim. Cosmochim. Acta 62, 2863–2886.

Mallmann, G., O'Neill, H.S.C., 2009. The crystal/melt partitioning of V during mantle melting as a function of oxygen fugacity compared with some other elements (Al, P, Ca, Sc, Ti, Cr, Fe, Ga, Y, Zr and Nb). J. Petrol. 50, 1765–1794.

Mason, B., Jarosewich, E., Melson, W.G., 1972. Mineralogy, petrology, and chemical composition of lunar samples 15085, 15256, 15271, 15475, 15476, 15535, 15555, and 15556. In: Proceedings of the Lunar Science Conference, vol. 3, pp. 785–796.

Mastrobuono-Battisti, A., Perets, H.B., Raymond, S.N., 2015. A primordial origin for the compositional similarity between the Earth and the Moon. Nature 520, 212.

McDonough, W.F., Sun, S.S., 1995. The composition of the Earth. Chem. Geol. 120, 223–253.

Millet, M.-A., Dauphas, N., Greber, N.D., Burton, K.W., Dale, C.W., Debret, B., Macpherson, C.G., Nowell, G.M., Williams, H.M., 2016. Titanium stable isotope investigation of magmatic processes on the Earth and Moon. Earth Planet. Sci. Lett. 449, 197–205.

Mougel, B., Moynier, F., Gopel, C., 2018. Chromium isotopic homogeneity between the Moon, the Earth, and enstatite chondrites. Earth Planet. Sci. Lett. 481, 1–8.

Neal, C.R., Taylor, L.A., 1992. Petrogenesis of mare basalts – a record of lunar volcanism. Geochim. Cosmochim. Acta 56, 2177–2211.

Nielsen, S.G., Prytulak, J., Halliday, A.N., 2011. Determination of precise and accurate V-51/V-50 isotope ratios by MC-ICP-MS, part 1: chemical separation of vanadium and mass spectrometric protocols. Geostand. Geoanal. Res. 35, 293–306.

Nielsen, S.G., Prytulak, J., Wood, B.J., Halliday, A.N., 2014. Vanadium isotopic difference between the silicate Earth and meteorites. Earth Planet. Sci. Lett. 389, 167–175.

Nielsen, S.G., Owens, J.D., Horner, T.J., 2016. Analysis of high-precision vanadium isotope ratios by medium resolution MC-ICP-MS. J. Anal. At. Spectrom. 31, 531–536.

Nielsen, S.G., Auro, M., Righter, K., Davis, D., Prytulak, J., Wu, F., Owens, J.D., 2019. Nucleosynthetic vanadium isotope heterogeneity of the early solar system recorded in chondritic meteorites. Earth Planet. Sci. Lett. 505, 131–140.

O'Neill, H.S.C., Navrotsky, A., 1984. Cation distributions and thermodynamic properties of binary spinel solid-solutions. Am. Mineral. 69, 733–753.

Pahlevan, K., Stevenson, D.J., 2007. Equilibration in the aftermath of the lunar-forming giant impact. Earth Planet. Sci. Lett. 262, 438–449.

Pahlevan, K., Stevenson, D.J., Eiler, J.M., 2011. Chemical fractionation in the silicate vapor atmosphere of the Earth. Earth Planet. Sci. Lett. 301, 433–443.

Papike, J.J., Hodges, F.N., Bence, A.E., Cameron, M., Rhodes, J.M., 1976. Mare basalts – crystal-chemistry, mineralogy, and petrology. Rev. Geophys. 14, 475–540.

Papike, J.J., Karner, J.M., Shearer, C.K., 2005. Comparative planetary mineralogy: valence state partitioning of Cr, Fe, Ti, and V among crystallographic sites in olivine, pyroxene, and spinel from planetary basalts. Am. Mineral. 90, 277–290.

Perron, C., 1976. Cross sections for production of stable and long-lived nuclides by high energy spallation of iron; cosmic ray implications. Phys. Rev. C 14 (3), 1108–1120.

Prytulak, J., Nielsen, S.G., Halliday, A.N., 2011. Determination of precise and accurate V-51/V-50 isotope ratios by multi-collector ICP-MS, part 2: isotopic composition of six reference materials plus the Allende chondrite and verification tests. Geostand. Geoanal. Res. 35, 307–318.

Prytulak, J., Nielsen, S.G., Ionov, D.A., Halliday, A.N., Harvey, J., Kelley, K.A., Niu, Y.L., Peate, D.W., Shimizu, K., Sims, K.W.W., 2013. The stable vanadium isotope composition of the mantle and mafic lavas. Earth Planet. Sci. Lett. 365, 177–189.

Prytulak, J., Sossi, P.A., Halliday, A.N., Plank, T., Savage, P.S., Woodhead, J.D., 2017. Stable vanadium isotopes as a redox proxy in magmatic systems? Geochem. Perspect. Lett. 3, 75–84.

Qi, Y., Wu, F., Ionov, D., Puchtel, I., Nicklas, R., Yu, H., Kang, J., Li, C., Huang, F., 2018. The vanadium isotopic composition of the BSE: constraints from peridotites and komatiites. In: Goldschmidt Abstracts, 2088.

Qin, L.P., Alexander, C.M.O., Carlson, R.W., Horan, M.F., Yokoyama, T., 2010. Contributors to chromium isotope variation of meteorites. Geochim. Cosmochim. Acta 74, 1122–1145.

Reufer, A., Meier, M.M.M., Benz, W., Wieler, R., 2012. A hit-and-run giant impact scenario. Icarus 221, 296–299.

Rufu, R., Aharonson, O., Perets, H.B., 2017. A multiple-impact origin for the Moon. Nat. Geosci. 10, 89–94.

Ryder, G., Schuraytz, B.C., 2001. Chemical variation of the large Apollo 15 olivine–normative mare basalt rock samples. J. Geophys. Res., Planets 106, 1435–1451.

Schauble, 2004. Applying stable isotope fractionation theory to new systems. Rev. Mineral. Geochem. 55, 65–111.

Scherer, P., Herrmann, S., Schultz, L., 1998. Noble gases in twenty-one Saharan LL-chondrites: exposure ages and possible pairings. Meteorit. Planet. Sci. 33, 259–265.

Sedaghatpour, F., Teng, F.Z., Liu, Y., Sears, D.W.G., Taylor, L.A., 2013. Magnesium isotopic composition of the Moon. Geochim. Cosmochim. Acta 120, 1–16.

Seifert, S., Ringwood, A.E., 1988. The lunar geochemistry of chromium and vanadium. Earth Moon Planets 40, 45–70.

Sossi, P.A., Bullet, J.P., O'Neill, H.S.C., 2018. Experimental calibration of vanadium partitioning and stable isotope fractionation between hydrous granitic melt and magnetite at 800 degrees C and 0.5 GPa. Contrib. Mineral. Petrol. 173, 27.

Sossi, P.A., Moynier, F., 2017. Chemical and isotopic kinship of iron in the Earth and Moon deduced from the lunar Mg-Suite. Earth Planet. Sci. Lett. 471, 125–135.

Sossi, P.A., Moynier, F., Chaussidon, M., Villeneuve, J., Kato, C., Gounelle, M., 2017. Early Solar System irradiation quantified by linked vanadium and beryllium isotope variations in meteorites. Nat. Astron. 1, 0055.

Stauffer, H., Honda, M., 1961. Cosmic-ray-produced V50 and K40 in the iron meteorite Aroos. J. Geophys. Res. 66, 3584–3586.

Wiesli, R.A., Beard, B.L., Taylor, L.A., Johnson, C.M., 2003. Space weathering processes on airless bodies: Fe isotope fractionation in the lunar regolith. Earth Planet. Sci. Lett. 216, 457–465.

Wood, B.J., Wade, J., Kilburn, M.R., 2008. Core formation and the oxidation state of the Earth: additional constraints from Nb, V and Cr partitioning. Geochim. Cosmochim. Acta 72, 1415–1426.

Wu, F., Qi, Y., Perfit, M.R., Gao, Y., Langmuir, C.H., Wanless, V.D., Yu, H., Huang, F., 2018. Vanadium isotope compositions of mid-ocean ridge lavas and altered oceanic crust. Earth Planet. Sci. Lett. 493, 128–139.

Wu, F., Qi, Y.H., Yu, H.M., Tian, S.Y., Hou, Z.H., Huang, F., 2016. Vanadium isotope measurement by MC-ICP-MS. Chem. Geol. 421, 17–25.

Xue, Y., Li, C.-H., Zhang, C., Miao, B., Huang, F., 2018. The vanadium isotopic composition of L ordinary chondrites. Acta Geochim. 501, 508.

Young, E.D., Kohl, I.E., Warren, P.H., Rubie, D.C., Jacobson, S.A., Morbidelli, A., 2016. Oxygen isotopic evidence for vigorous mixing during the Moon-forming giant impact. Science 351, 493–496.

Zhang, J.J., Dauphas, N., Davis, A.M., Leya, I., Fedkin, A., 2012. The proto-Earth as a significant source of lunar material. Nat. Geosci. 5, 251–255.